

Asymmetric Complementary Interface for Directional Adhesion

Zhen Yang

Department of Mechanical Engineering, 4-225 Donadeo Innovation Centre for Engineering, 9211-116 Street NW, Edmonton, AB T6G 1H9, Canada

Congrui Jin

Department of Mechanical Engineering, Binghamton University, 4400 Vestal Pkwy E Binghamton, NY 13902, USA

Tian Tang*

Department of Mechanical Engineering, 10-203 Donadeo Innovation Centre for Engineering, 9211-116 Street NW, Edmonton, AB T6G 1H9, Canada

Abstract

Inspired by nature, structured interfaces have been shown to enhance adhesion by trapping crack propagation along the interface. In many applications, directional adhesion is desired where interface separation along different directions requires different fracture energy. In this work, we numerically investigate a strategy to attain enhanced and directional adhesion using an interface that contains asymmetric complementary patterns. Finite element analyses were performed to calculate the energy release rate at different crack lengths on the patterned interface, and the results were compared to those for a flat control. Our results show that the adhesion is stronger on the patterned

*Corresponding author. Email: tian.tang@ualberta.ca

interface and the adhesion enhancement is greater along one direction than the other, suggesting directional adhesion. Different degrees of directional adhesion can be achieved by modulating the aspect ratio of the pattern on the interface without modifying surface chemistry, which bears great potential in applications where different levels of adhesion and directional adhesion are desired for different purposes.

Keywords: Directional Adhesion, Energy Release Rate, Finite Element Analysis

1. Introduction

Adhesion plays important roles in numerous fields. There are examples in our everyday lives from clothing such as Velcro[1] to office supplies such as Post-it notes[2], and examples in engineering across multi-scales such as robotics[3], soft electronics[4][5] and biomimetic systems[6][7]. Conventionally, pressure-sensitive adhesives (PSAs) [8] have been used to achieve strong adhesion via high viscous dissipation on the interface. However, PSAs exhibit several drawbacks such as low repeatability and sensitivity to surface roughness. Other more permanent adhesives available in the market may have undesirable properties such as non-repeatability, requirement for surface chemical modification, and/or toxicity. To overcome the drawbacks of conventional adhesives, significant work has focused on the design of surface structure for enhanced and repeatable adhesion.

One way of introducing strong yet repeatable adhesion is inspired from nature by geckos' feet. It was shown by Autumn *et al.*[9] that there are

thousands of microscopic angled setae on a gecko's foot (e.g., Tokay gecko). The tip of each seta branches into hundreds of spatula terminals, leading to hierarchical fibrillar structures that conform to and form intimate contact with a wide range of surfaces regardless of their roughness. Several mechanisms have been proposed to contribute to the enhanced adhesion of fibrillar surfaces compared with unstructured surfaces. Jagota *et al.*[10] showed that when a crack propagates on a fibrillar interface, the fibrils previously located ahead of the crack tip get unloaded and the strain energy stored in these fibrils is dissipated instead of being released back to the bulk.

Later, Hui *et al.* [11] showed that an interfacial crack adjacent to fibrillar structure is blunted when it reaches a fiber, and the concentrated stress field at the crack tip is redistributed into an equal load sharing zone over a characteristic length much larger than the diameter of the fiber. Therefore, the stress concentration at the crack tip is significantly reduced, hindering the crack propagation. Using a cohesive zone model, Tang *et al.* [12] quantified the adhesion enhancement of a fibrillar interface. A dimensionless fiber radius χ was introduced to separate the flaw-sensitive and flaw-insensitive regimes of interface failure. When $\chi > 0.7$, the strength of a fibrillar interface increases with decreasing χ (decreasing fiber radius).

Based on the above understanding, numerous bio-inspired fibrillar surfaces have been created and compared with unstructured surfaces. Effects of fiber diameter, aspect ratio, spacing and tip geometries have been investigated [13][14][15][16][17]. Among them, Glassmaker *et al.* [17] discovered

that vertical fibrils with a thin layer of film connecting them can also lead to enhanced adhesion due to crack-trapping: the periodic microstructure near the interface results in reduction in the energy release rate G available for crack propagation; for G to reach the intrinsic work of adhesion, more energy is required externally and hence the apparent adhesion is enhanced.

While the above works investigated the adhesion between a structured surface and a smooth surface, there have also been studies where structural modification was done on both sides of the interface, e.g., using complementary surfaces. One inherent advantage associated with such an interface is that the adhesion is highly selective: only when the upper and lower surfaces have complementary patterns and are well aligned can enhanced adhesion be achieved during the separation. Shilpi *et al.* [18] conducted experiments to measure the adhesion between two PDMS sheets that contain complementary rippled structures described by a sinusoidal function. During the experiments, the two sheets were first pushed together and then separated by inserting a wedge into the interface. A separate finite element(FE) model with the same dimensions as the actual sample was created to evaluate the energy release rate at the crack tip as it propagates through the interface. The FE model is subjected to a uniform displacement along the top edge to mimic a mode I loading. The FE results indicated that the energy release rate G is reduced when the crack tip moves in directions other than horizontal, and periodically undulates with the apparent crack tip location. The ratio between the local minima of G on a rippled interface and G in a

flat control is calculated at the same apparent crack tip location. Then the adhesion enhancement in the rippled interface was assessed by the inverse of this ratio. The adhesion is enhanced due to the same crack trapping mechanism as mentioned in Glassmaker *et al.* [17], and was shown to increase with increasing amplitude of the ripple.

Later, Singh *et al.*[19] investigated the adhesion in a PDMS interface with complementary pillars and channels. Similar to the study of the rippled interface [18], a FE model was created to evaluate the energy release rate at the crack tip, when the sample was subjected to a uniform displacement on the top. The FE results showed that the adhesion enhancement for the pillar/channel interface is approximately 5 times and is independent of the pillar height.

In many engineering applications, directional adhesion is desired where interface separation along different directions requires different fracture energy. One such example is climbing robot (*stickybot*, [3]), which needs strong adhesion to stick its feet on vertical surfaces and weak adhesion to detach the feet while walking. The directional adhesion in *stickybot* was enabled by angled polymer fibrils on its feet pad: when loaded against the preferred direction, the structure exhibits friction with no adhesion; when loaded in the preferred direction, the structure exhibits adhesion in both normal and shear directions. Another potential application of directional adhesion is in the recycling of spent lithium-ion batteries, which can provide significant economic and environmental benefits. Although diverse process chains have

been applied to recycle batteries, a critical issue for the recycling of battery electrodes is the separation of the current collector from the composite film. Since the delamination between the current collector and the composite film often causes battery failure, many strategies have been developed to increase the interfacial adhesion between them [20][21][22]. Those techniques indeed lead to enhanced battery lifetime, but they make the battery recycling more challenging. It is desirable to have an interface between the current collector and the composite film which displays directional adhesion, i.e., significantly enhanced adhesion can be obtained during its lifetime to combat delamination, whereas during recycling, the composite film can be easily peeled off from the current collector along a certain direction. While angled fibrils in *stickybot* can produce directional adhesion, they also reduce the contact area and create some cavities in the bulk material near the interface, which is not desirable for some applications such as lithium-ion battery. Furthermore, there are other issues related to fibrils such as the collapse and adhesion between them, which weakens interface adhesion. In this paper, we explore another strategy to induce enhanced and directional adhesion, motivated by the adhesion enhancement of complementary patterned interfaces. In the works by Shilpi *et al.* [18] and Singh *et al.* [19], no directional adhesion is expected as the interface patterns used are symmetric, i.e., there is no difference for the crack to propagate from the two opposite directions. In this work, the above symmetric interface patterns are replaced by asymmetric triangles separated by flat regions, which are expected to lead to different adhesion

enhancements along different separation directions. Through an in-depth numerical investigation and detailed parametric study, we not only demonstrate the feasibility of generating directional adhesion using the proposed interface, but also provide mechanistic understanding and design suggestions on the function of such interface.

The rest of the paper is organized as follows. Section 2 presents details about the geometry studied and FE modelling. In Section 3, FE results for asymmetric complementary interfaces under different loading conditions are discussed, to investigate directional adhesion. Section 4.1 discusses the modulation of directional adhesion by adjusting the pattern geometry. Finally, conclusions are given in Section 5.

2. Finite element models

The commercial package ABAQUS was used for the finite element analysis (FEA). Figure 1 shows the schematic of a patterned interface model that contains right triangles separated by flat regions. A completely flat interface model (not shown) serves as a control which also has the same apparent length (L) and thickness ($2H$) as shown in Figure 1(a).

Because the triangular pattern is asymmetric, two opposite crack separation directions are examined. As the crack propagates from left to right (direction 1), it travels upwards along the vertical side of the triangle, and then downwards along the hypotenuse. As it propagates from right to left (direction 2), it travels upwards along the hypotenuse, and then downwards

along the vertical side. Along each direction, there is a flat region (length l_f shown in Figure 1(b)) before the separation of the patterned region. Figure 1(b) also illustrates the first three “kinks” in the patterned region where the crack propagation changes direction. They are denoted by A , B and C based on the sequence in which they are accessed by the crack tip. Subscripts 1 and 2 are used to denote different directions, for example A_1 corresponds to the first “kink” accessed by the crack tip when the crack is extended along direction 1.

Three types of loading conditions and associated boundary conditions are applied, as shown in Figure 1. In the first case (Figure 1(a) for crack propagation along direction 1), hereafter referred to as the pulling condition, the top boundary is subjected to a uniformly distributed displacement δ while the bottom edge is fixed in a “frictionless” manner. In the second case (Figure 1(b) for crack propagation along direction 1), hereafter referred to as the symmetric peeling condition, the first few nodes on the top and bottom edges are subjected to the uniform displacement δ . In the third case (Figure 1(c) for crack propagation along direction 1), hereafter referred to as the asymmetric peeling condition, the first few nodes on the top boundary is subjected to displacement δ and the bottom edge is constrained in a “frictionless” manner. The pulling condition mimicks the work of Shilpi [18] and Singh [19], while the two peeling conditions allow for additional investigation on how loading condition affects directional adhesion. Figure 1(d) shows how the displacement δ changes with numerical step n . From 0 to n_0 , δ increases

linearly. After $n = n_0$, δ remains constant ($\delta_0 = 1$ mm). As will be seen later, to evaluate the adhesion enhancement the energy release rate for the patterned interface will be normalized by that of a flat interface under the same applied displacement. So the results are insensitive to the actual value of δ_0 .

Each model consists of one upper part (above the interface) and one lower part (below the interface), which form frictionless and hard contact pairs. As well, the upper and lower interfacial surfaces contain the same number of nodes, and all the paired nodes along the interface are initially “tied” from steps 0 to n_0 . After n_0 , a crack propagation is mimicked by nodal release, where the paired nodes are released from the tie constraint step by step. In this fashion, the length of the crack is extended in the direction along which the tied nodes are released. During each numerical step $n(\geq n_0)$, the strain energy for the entire model U_n is recorded, and the strain energy release rate G is calculated by:

$$G = -\frac{dU}{da} \approx \frac{U_n - U_{n+1}}{a_{n+1} - a_n} \quad (1)$$

where a_n , referred to as the actual crack tip location at step n , is the total distance along the separated surfaces from A_1 in Figure 1(b) to the crack tip.

The material used for the FE models is polydimethylsiloxane(PDMS), modeled as an incompressible Neo-Hookean hyperelastic material. The strain energy density for incompressible Neo-Hookean material is given by $U = C_{10}(I_1 - 3)$, where I_1 is the first strain invariant of the left Cauchy-Green

deformation tensor. The value of coefficient C_{10} is obtained from an experimental work that measured the mechanical properties of PDMS[23], $C_{10} = 0.0705MPa$. Quad-dominated mesh scheme and plane stress elements are applied to all models.

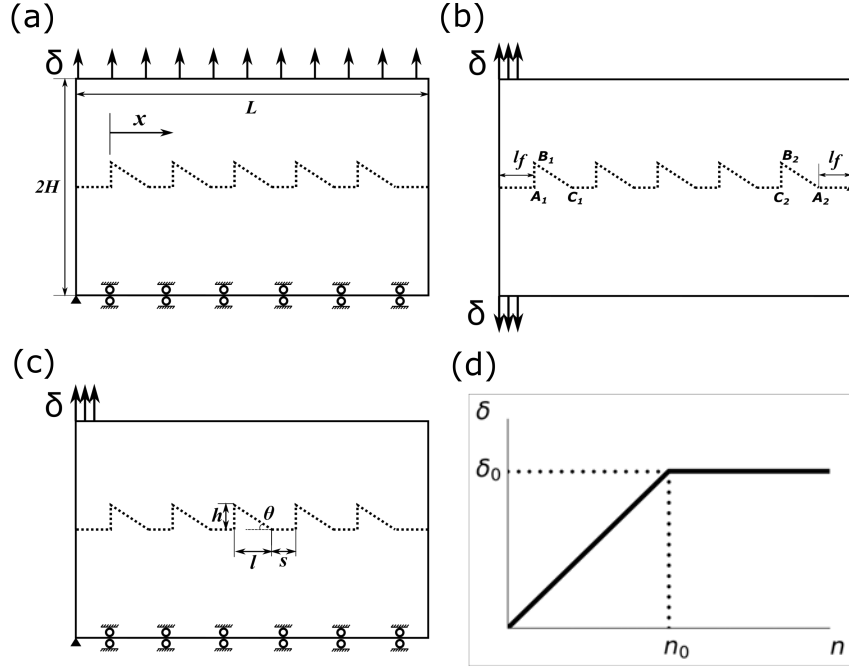


Figure 1: The three types of loading and boundary conditions applied to the FE models: (a) pulling, (b) symmetric peeling and (c) asymmetric peeling. (d) shows how the displacement δ changes with numerical step n . To clearly show the definition of geometric parameters, the patterns are not drawn to scale.

3. Directional adhesion with asymmetric interface

The purpose of this section is to investigate whether the adhesion is enhanced by the patterned interface compared with a flat one, and whether the

enhancement is different along different directions. Thus, geometrical parameters are fixed as: $H/l = 3.5$, $\theta = \frac{\pi}{6}$, $s/L = 0.09$ and $L/H = 15.6$ (refer to Figure 1 for their definitions), while two opposite crack separation directions are examined. To mimick a thin layer of adhesives, the lateral length (L) of the sample is set to be much larger than the thickness H as well as the dimensions of the triangular teeth. The results under pulling condition will be presented first, followed by those under symmetric and asymmetric peeling conditions.

3.1. Pulling

Figure S1 (Supplementary Material) shows the schematics of the interface under pulling as the crack propagates from left to right (pulling direction 1) and from right to left (pulling direction 2). Energy release rate on the patterned interface ($G_{pattern}$) and that on the flat interface (G_{flat}) are calculated by gradually releasing the “tied” nodes. Figure 2 shows $G_{pattern}$ and G_{flat} versus the normalized actual crack location a/λ_a along pulling direction 1. λ_a is defined as $\lambda_a = h + \frac{l}{\cos(\theta)} + s$, which represents the actual length of the interface in each period of the pattern (see Figure 1(c)). Since the projection of any points along the vertical path from A_1 to B_1 (see Figure 1(b)) onto the flat interface is a single point, in this region, a/λ_a increases but G_{flat} is constant, as shown in the enlarged inset of Figure 2. As can be seen in Figure 2, before the crack reaches the pattern the interface is flat and $G_{pattern}$ is identical to G_{flat} . It then deviates from G_{flat} and shows discontinuity

when the crack propagation changes direction in the patterned region. In the flat region between the triangles, $G_{pattern}$ and G_{flat} have close values, but are not identical. In the triangular region, $G_{pattern}$ can become significant smaller than G_{flat} . If the crack in the flat control propagates in a quasi-static manner, i.e., $G_{flat} = W_{ad}$ (the intrinsic work of adhesion of the interface), Figure 2 suggests that the pattern has led to smaller $G_{pattern}$ compared to $G_{flat}(= W_{ad})$, hence the crack is trapped. For the crack to further propagate, more energy input is required for the local minima of $G_{pattern}$ to reach W_{ad} , and the apparent adhesion is enhanced.

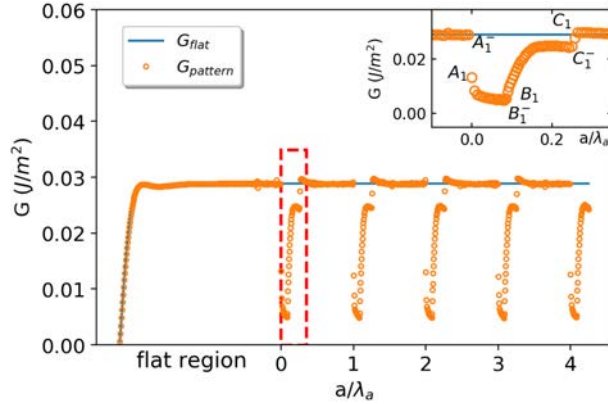


Figure 2: $G_{pattern}$ and G_{flat} versus the normalized actual crack tip location a/λ_a for pulling direction 1. The inset shows the enlarged plot of the boxed region.

To compare $G_{pattern}$ and G_{flat} in more detail, it is convenient to introduce an energy release rate ratio, $R = \frac{G_{pattern}}{G_{flat}}$. Results for the two pulling directions are shown in the left and right panels of Figure 3, respectively. The color grey is used to highlight regions where $R > 1$, while blue is used to highlight regions with $R \leq 1$. Figure 3(a) and (b) show the schematics of the

interface as the crack propagates in pulling directions 1 and 2. Figure 3(c) and (d) show how R changes with the normalized apparent crack tip location x/λ_x . Here x is the apparent crack tip location defined as the projected length of the interface onto the horizontal direction measured from point A_1 in Figure 1(b) to the crack tip. λ_x is defined as $\lambda_x = l + s$, representing the apparent or horizontally projected length of the interface in each period of the pattern. Figure 3(e) and (f) show the enlarged plots of the boxed regions in (c) and (d), but re-plotted against the normalized actual crack tip location a/λ_a . The superscript “ $-$ ” is used to denote the location just prior to the “kinks” in the pattern. For example, B_1^- refers to the location one node prior to B_1 .

In the case of pulling direction 1 shown in the left panel of Figure 3, from the leftmost end to A_1^- the crack is horizontal and R is equal to 1. Between A_1^- and A_1 , R experiences an abrupt decrease from 1 to 0.45. From A_1 to B_1^- , the crack surface is vertical (vertical-up) and R decreases further from 0.45 to 0.17. Between B_1^- and B_1 , R slightly increases from 0.17 to 0.23. From B_1 to C_1^- , the crack surface has an angle of 30° below horizontal (ramping-down) and R increases from 0.23 to a plateau value of 0.81. Between C_1^- and C_1 , R slightly increases from 0.81 to 0.94. From C_1 in $0 < x/\lambda_x < 1$ to A_1^- in $1 < x/\lambda_x < 2$ (the first kink in the second period of the pattern; the same notation will be used hereafter), the crack surface is flat again; R first increases from 0.94 to 1.02 and then decreases to 1. From $0 < x/\lambda_x < 1$ to $x/\lambda_x \geq 4$, the R curve shows periodic pattern but with variations in the

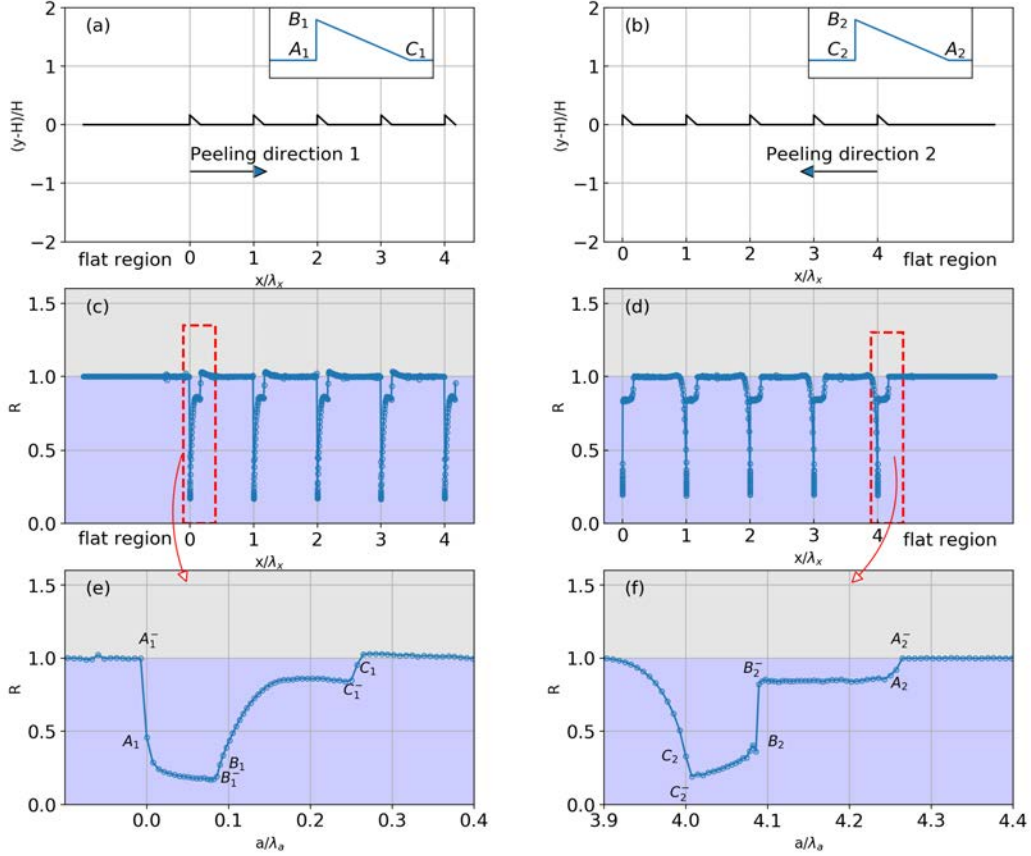


Figure 3: Energy release rate ratio R for the two different pulling directions, left panel: pulling direction 1; right panel: pulling direction 2. (a) and (b) are schematics of the interface. (c) and (d) are R versus the normalized apparent crack tip location x/λ_x . (e) and (f) are R versus the normalized actual crack tip location a/λ_a for the boxed regions in (c) and (d) respectively.

R_{min} values.

In the case of pulling direction 2 shown in the right panel of Figure 3, from the rightmost end to A_2^- , the crack surface is horizontal and R is equal to 1. Between A_2^- and A_2 , R slightly decreases from 1 to 0.90. From A_2 to B_2^- , the crack surface has an angle of 30° above horizontal (ramping-up) and R decreases to a plateau value of 0.80. Between B_2^- and B_2 , R experiences

an abrupt decrease from 0.80 to 0.33. From B_2 to C_2^- , the crack surface is vertical (vertical-down) and R decreases from 0.33 to 0.19. Between C_2^- and C_2 , R slightly increases from 0.19 to 0.33. From C_2 to A_2^- in $3 < x/\lambda_x < 4$, the crack surface is flat; R increases from 0.33 to 1 and remains at this value. From $x/\lambda_x \geq 4$ to $0 < x/\lambda_x < 1$, the R curve shows periodic pattern but with slight variations in the R_{min} values.

Several similarities can be observed between the results from the two pulling directions. Firstly, R curves show discontinuities at “kinks” where the crack propagation changes direction. Secondly, R in the first flat region is constant and equal to 1. In later periods it deviates from 1 in the triangular regions but approaches 1 as the crack tip moves away from the “kinks”. Despite the above similarities, several differences can be observed. Firstly, the local minima of R (R_{min}) occurs at different locations along the two directions. R_{min} for pulling direction 1 occur in the vicinity of kink B_1 while those for pulling direction 2 occur in the vicinity of kink C_2 , as Figure 4(a) illustrates. Secondly, there is a small quantitative difference in the R_{min} values. R_{min} varies in the range of 0.16 to 0.17 for pulling direction 1 and in the range of 0.19 to 0.20 for pulling direction 2. Because R_{min} correspond to the maximum reduction in $G_{pattern}$ when the patterned interface is under the same loading as the flat interface, an adhesion enhancement factor can be defined as:

$$F = \begin{cases} \frac{1}{R_{min}}, & \text{in the patterned region} \\ 1, & \text{otherwise} \end{cases} \quad (2)$$

which is a measure of how much the adhesion is enhanced compared to a flat interface. Figure 4(b) shows the adhesion enhancement factor F calculated by Eqn.(2) for the two pulling directions. F for pulling direction 1 ranges from 5.8 to 6.0 while that for pulling direction 2 varies between 5.0 and 5.2, indicating weak directional adhesion. The variation of F with the apparent crack tip location is small for each direction because of the periodic R_{min} curves.

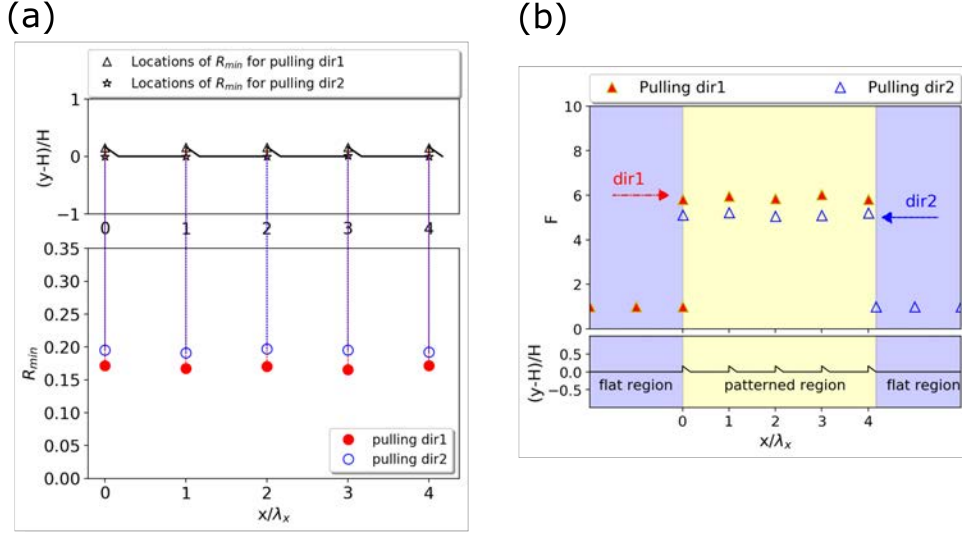


Figure 4: (a) R_{min} for pulling directions 1 and 2, plotted against the normalized apparent crack tip location where R_{min} occurs. (b) Adhesion enhancement factor F for pulling directions 1 and 2, plotted against the normalized apparent crack tip location where R_{min} occurs.

An approximate analytical solution to the adhesion enhancement in a patterned interface under pulling was proposed by Shilpi [18] and Singh [19] as $F = [\cos(\frac{\alpha_{max}}{2})]^{-4}$ where α_{max} is the maximum tangential angle of the interface. If this equation were used for the pattern considered here, F

would be predicted to be $1/\cos^4(\frac{\theta_{max}}{2}) = 1/\cos^4(\frac{90^\circ}{2}) = 4$ where $\theta_{max} = 90^\circ$ is the angle between the future crack surface and the horizontal direction at locations where R_{min} occurs. However, F shown in Figure 4(b) is higher along both pulling directions. The deviation is caused by two strong assumptions upon which the analytical solution was derived: 1) the crack is embedded in an infinite body and 2) the surface before the crack tip is horizontal. In our case, however, the model is of finite size and as the crack propagates its length can become comparable to the apparent length of the sample. In addition, the surface before the crack tip locations where R_{min} occurs is not horizontal (vertical from A_1 to B_1 along direction 1 and slanted from A_2 to B_2 along direction 2).

3.2. Symmetric peeling

Figure S2 (Supplementary Material) shows the schematics of the interface under symmetric peeling as the crack propagates from left to right (peeling direction 1) and from right to left (peeling direction 2). Figure 5 shows $G_{pattern}$ and G_{flat} versus the normalized actual crack tip location a/λ_a . Similar to Figure 2, before the crack reaches the pattern the interface is flat and $G_{pattern}$ is identical to G_{flat} . It then deviates from G_{flat} and shows discontinuity when the crack reaches the patterned region and changes propagation direction. In the flat region between the triangles, $G_{pattern}$ is close to G_{flat} but not identical. In the triangle regions, $G_{pattern}$ can become significantly smaller than G_{flat} , thus the apparent adhesion is enhanced due to crack-

trapping. One big difference from Figure 2 is that both $G_{pattern}$ and G_{flat} show an overall decreasing trend at large a/λ_a , which is not observed in Figure 2.

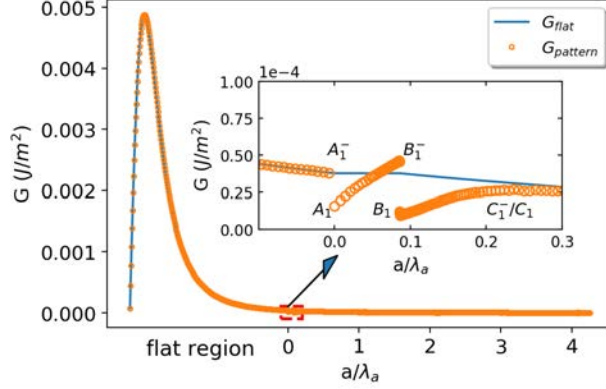


Figure 5: $G_{pattern}$ and G_{flat} versus the normalized actual crack tip location a/λ_a under symmetric peeling for peeling direction 1.

The R curves for the two peeling directions are shown in the left and right panels of Figure 6, respectively. Figure 6(a) and (b) show the schematics of the interface as the crack propagates in peeling directions 1 and 2. Figure 6(c) and (d) show how R changes with the normalized apparent crack tip location x/λ_x . Figure 6(e) and (f) show the enlarged plots of the boxed regions in (c) and (d), but re-plotted against the normalized actual crack tip location a/λ_a .

In the case of peeling direction 1 shown in the left panel of Figure 6, from the leftmost end to A_1^- the crack is horizontal and R is equal to 1. Between A_1^- and A_1 , R experiences an abrupt decrease from 1 to 0.42. From A_1 to B_1^- , the crack surface is vertical (vertical-up) and R increases from 0.42 to

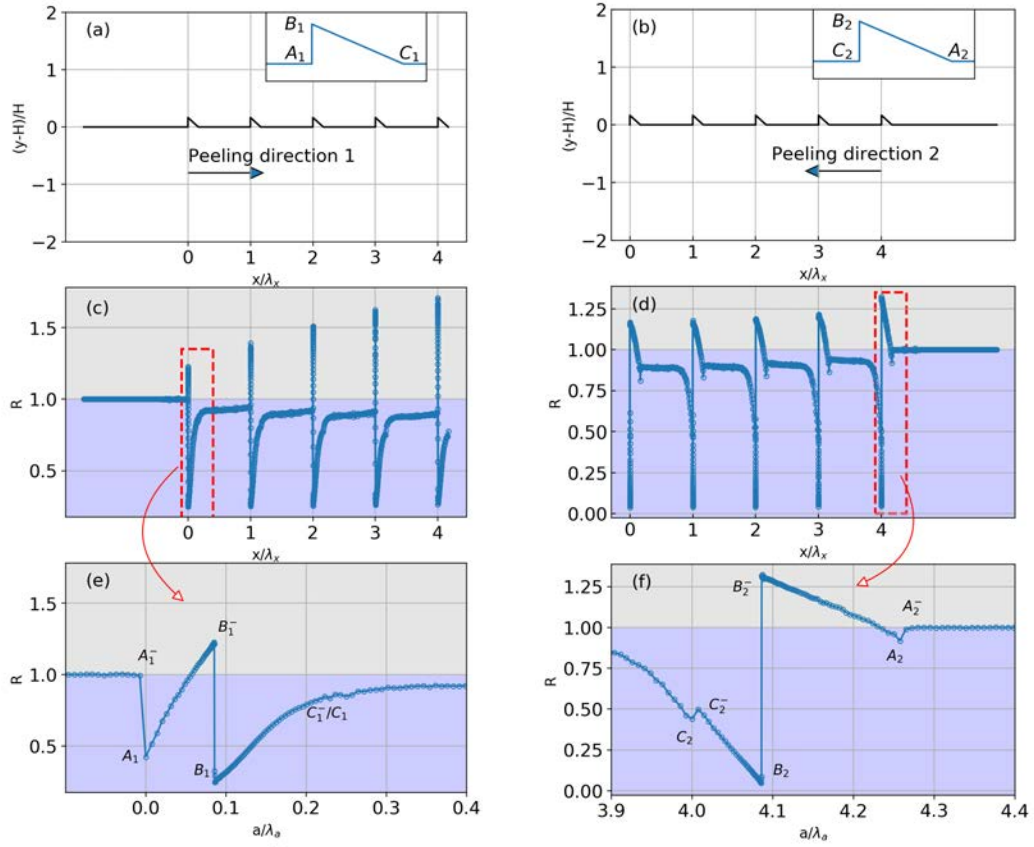


Figure 6: Energy release rate ratio R for the two different symmetric peeling directions, left panel: peeling direction 1; right panel: peeling direction 2. (a) and (b) are schematics of the interface. (c) and (d) are R versus the normalized apparent crack tip location x/λ_x . (e) and (f) are enlarged regions in (c) and (d), versus the normalized actual crack tip location a/λ_a .

1.22. Between B_1^- and B_1 , R suddenly decreases from 1.22 to 0.33 and then further decreases to a local minimum 0.25 as the crack propagates by a few crack lengths. From the local minimum location to C_1^- , the crack surface has an angle of 30° below horizontal (ramping-down) and R increases from 0.25 to 0.81. Between C_1^- and C_1 , R slightly increases from 0.81 to 0.82. From C_1 in $0 < x/\lambda_x < 1$ to A_1^- in $1 < x/\lambda_x < 2$, the crack surface is flat again yet R is not constant, instead it increases from 0.82 to a plateau value of 0.95. From $0 < x/\lambda_x < 1$ to $x/\lambda_x \geq 4$, the R curve shows periodic pattern but its magnitude varies from one period to another.

In the case of peeling direction 2 shown in the right panel of Figure 6, from the rightmost end to A_2^- , the crack surface is horizontal and R is equal to 1. Between A_2^- and A_2 , R slightly decreases from 1 to 0.92. From A_2 to B_2^- , the crack surface has an angle of 30° above horizontal (ramping-up) and R increases from 0.92 to 1.30. Between B_2^- and B_2 , R experiences an abrupt decrease from 1.30 to 0.09 and then further decreases to a local minimum 0.05 as the crack propagate by a few crack lengths. From the local minimum location to C_2^- , the crack surface is vertical (vertical-down) and R increases from 0.05 to 0.49. Between C_2^- and C_2 , R slightly decreases from 0.49 to 0.44. From C_2 to A_2^- in $3 < x/\lambda_x < 4$, the crack surface is flat while R increases from 0.44 to a plateau value of 0.93. From $x/\lambda_x \geq 4$ to $0 < x/\lambda_x < 1$, the R curve shows periodic pattern but variations in its magnitude.

There are clear similarities between the results from the two peeling directions. For both peeling directions the R curves show discontinuities at

'kinks' where the crack propagation changes direction. While R in the first flat region is constant and equal to 1, this does not hold in later flat regions. Lastly, Figure 7(a) shows R_{min} during each period versus x/λ_x where R_{min} occurs. As can be seen, R_{min} always occurs in the vicinity of kink B regardless of the peeling directions. Despite these qualitative similarities, there is substantial difference in the R_{min} values. R_{min} for peeling direction 1 varies in the range of 0.25 to 0.26 while R_{min} for peeling direction 2 varies in the range of 0.04 to 0.05. Using Eqn.(2), F for the two peeling directions are calculated and plotted in Figure 7(b) against x/λ_x where R_{min} occurs. In the flat regions before the patterned region, F is equal to 1 along both directions. In the patterned region F is in the range of 3.8 to 4.0 for peeling direction 1 and 21.0 to 26.0 for peeling direction 2, indicating strong directional adhesion. The adhesion enhancement factor for peeling direction 2 is approximately 6 times higher than that for peeling direction 1. In addition, F for peeling direction 2 have a much greater variation with respect to the normalized crack tip location.

To explain the directional adhesion, we carefully investigated the regions in the vicinity of kink B in the first period where R_{min} occur. In Figure 8(a), the crack tip is considered to be at B_1 and to be propagated to B_1^+ along direction 1. Here, the superscript "+" is used to denote the location just after the 'kink' in the pattern, i.e., B_1^+ refers to the location one node after B_1 . The corresponding scenario for direction 2 is shown in Figure 8(b).

Figure 8(a) also shows the upper and lower surfaces ahead of B_1^+ , denoted

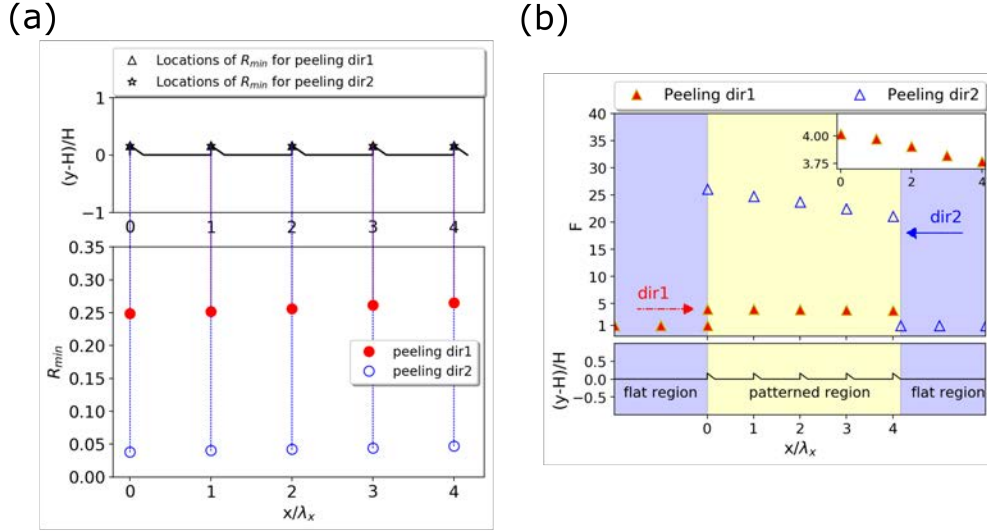


Figure 7: (a) R_{min} for symmetric peeling directions 1 and 2, plotted against the normalized apparent crack tip location where R_{min} occurs. (b) Adhesion enhancement factor F for symmetric peeling directions 1 and 2, plotted against the normalized apparent crack tip location where R_{min} occurs.

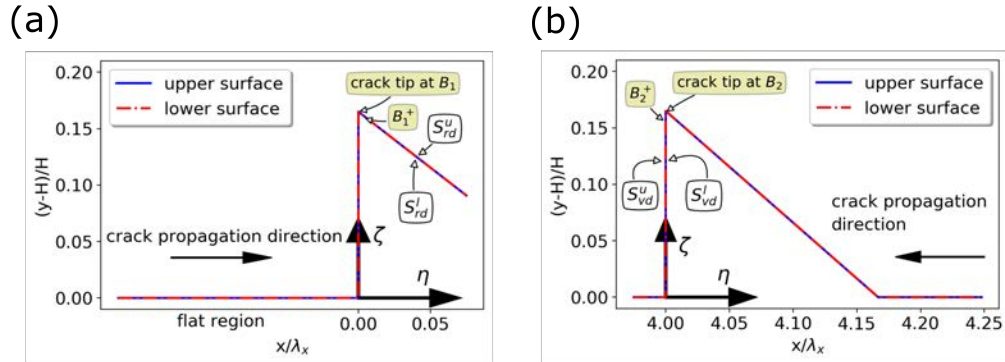


Figure 8: Schematics of the two surfaces when the crack tips are at B_1 and B_2 to be propagated to B_1^+ and B_2^+ , respectively for peeling directions 1 and 2.

by S_{rd}^u and S_{rd}^l respectively where the subscript rd indicates the ramping-down portion of the pattern. A coordinate system η - ζ is introduced as shown with its origin at the bottom of the vertical-up surface. Then the following

auxiliary simulations (Cases-1a,1b and 1c) were performed to investigate the deformation of S_{rd}^u and S_{rd}^l under several loading conditions.

Case-1a: The displacement δ in Figure S2(a) is only applied to the top edge while the bottom edge is fixed. The crack tip is allowed to propagate from B_1 to B_1^+ .

Case-1b: δ in Figure S2(a) is only applied to the bottom edge while the top edge is fixed. The crack tip is allowed to propagate from B_1 to B_1^+ .

Case-1c: δ in Figure S2(a) is applied to both top and bottom edges. The crack is allowed to propagate from B_1 to B_1^+ . It returns to the problem of symmetric peeling.

The deformed S_{rd}^u and S_{rd}^l are shown in Figure 9 for the three cases, along with their undeformed shape for comparison. Regions near the crack tips in the three cases are enlarged on the right. For Case-1a, peeling the upper part alone causes S_{rd}^u to deform toward the top-right direction, i.e. away from S_{rd}^l . Hence, a separation at the crack tip is introduced. Similarly, peeling the lower part alone causes S_{rd}^l to deform toward the bottom-left direction, away from S_{rd}^u , leading to a separation at the crack tip in Case-1b. Since individual peeling of the upper and lower parts both open up the crack at B_1^+ , in Case-1c the two effects combine to drive larger opening of the crack. The contribution from individually peeling the upper surface is greater than individually peeling the lower surface, evidenced by the much larger crack opening in Case-1a compared with Case-1b. It should be pointed out that in Case-1c, one point on the right boundary of the sample is fixed to prevent

rigid body translation (see Figure 1(b)), whereas in Case-1a and Case-1b, the entire bottom or top edge of the model is fixed in the vertical direction (see Figure 1(c) for Case-1a). As a result, the model is less constrained in Case-1c, and slight rigid body rotation can occur when the crack propagates in the asymmetrically patterned region where the upper and lower parts have locally unequal thicknesses. This is why the deformed surface in Case-1c as seen in Figure 9 is located below both Case-1a and Case-1b.

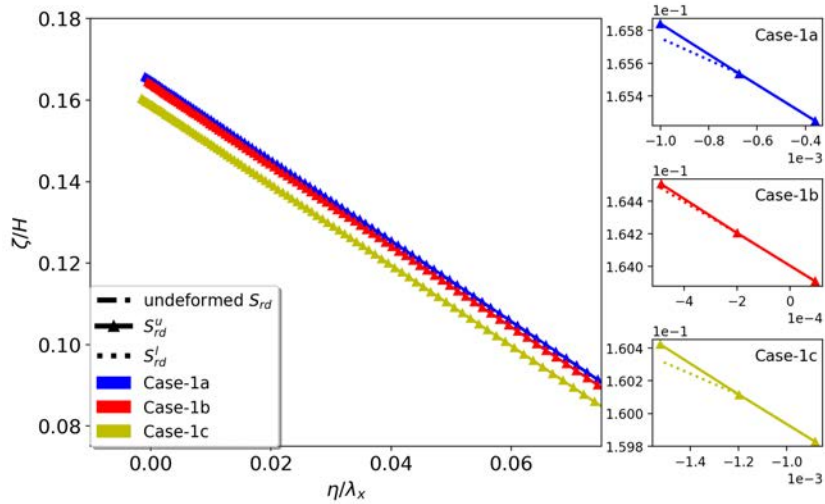


Figure 9: Deformed and undeformed S_{rd}^u and S_{rd}^l in Case-1a, 1b and 1c. Regions near the crack tips for the three cases are enlarged on the right. Note that the deformation of the tooth is small, and the undeformed S_{rd}^u and S_{rd}^l almost overlap with the deformed shape for Case-1a in the left figure.

Figure 8(b) shows the upper and lower surfaces ahead of B_2^+ in the undeformed state for peeling direction 2. S_{vd}^u and S_{vd}^l are used to denote the upper and lower surfaces ahead of the crack tip, along the vertical-down portion of the pattern. Similarly to Figure 8(a), coordinate system $\eta - \zeta$ is introduced with its origin at the bottom end of S_{vd} . We again performed auxiliary sim-

ulations (Cases-2a, 2b and 2c) to investigate the deformation of S_{vd}^u and S_{vd}^l under several loading conditions.

Case-2a: δ in Figure S2(b) is only applied to the top edge while the bottom edge is fixed.

Case-2b: δ in Figure S2(b) is only applied to the bottom edge while the top edge is fixed.

Case-2c: δ in Figure S2(b) is applied to both top and bottom edges.

In each case, the crack tip is allowed to propagate from B_2 to B_2^+ , and Case-2c returns to the problem of symmetric peeling.

The deformed S_{vd}^u and S_{vd}^l are shown in Figure 10 for the three cases, along with their undeformed shape for comparison. Regions near the crack tips in the three cases are enlarged on the right. For Case-2a, peeling the upper part causes S_{vd}^u to deform to the right, i.e. towards S_{vd}^l . The triangular tooth adjacent to S_{vd}^l then plays a role of resisting the deformation of S_{vd}^u . As a result, the crack between S_{vd}^u and S_{vd}^l is “closed”. The crack closing is associated with slight material interpenetration, as can be seen from the enlarged Case-2a result in Figure 10, since the surfaces in the FE model are defined to be in hard contact with a stiffness penalty function. This numerical treatment allows for finite interpenetration under significant compressive contact. In Case-2b, peeling the lower part causes S_{vd}^l to deform to the right, away from S_{vd}^u and opening the crack. Unlike peeling direction 1, along peeling direction 2 loadings on the upper and lower parts have opposite effects on crack propagation. Consequently, when both parts are peeled in Case-2c,

the two effects compete leading to an overall small crack opening. Similar to Figure 9, the deformed surface in Case-2c is below Case-2a and Case-2b in Figure 10, because of the stronger boundary constraint in the latter two cases.

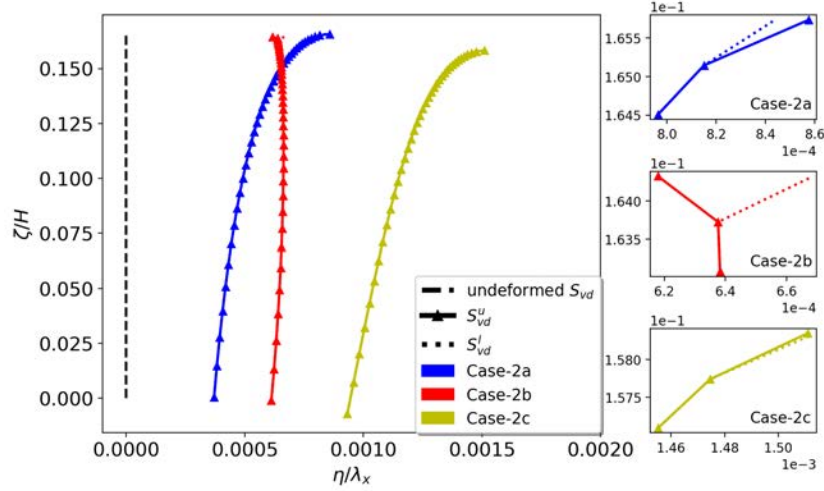


Figure 10: Deformed and undeformed S_{vd}^u and S_{vd}^l in Case-2a, 2b and 2c. Regions near the crack tips for the three cases are enlarged on the right. Compare to Figure 9, the deformation of the tooth is much more significant.

In summary, when the crack tip reaches the vicinity of kink B from different directions, peeling the upper or lower parts play different roles in the crack propagation: along direction 1, peeling upper and lower parts both contribute to crack propagation; along direction 2, peeling the lower part contributes to crack propagation whereas peeling the upper part contributes to crack trapping. The above analysis qualitatively explains why the R_{min} value in the vicinity of B is higher (or F is lower) along direction 1 than along direction 2. A quantitative evaluation of the stress field ahead of the

crack tip is also conducted for the two peeling directions and the details are given in Section S2 (Supplementary Material).

3.3. Asymmetric peeling

Figure S3 shows the schematics of the interface under asymmetric peeling, by fixing the bottom and peeling the top edge, the crack propagates from left to right (peeling direction 1) or from right to left (peeling direction 2); by fixing the top and peeling the bottom edge, the crack propagates from left to right (peeling direction 3) or from right to left (peeling direction 4).

The R curves for the four peeling directions are shown in Figures S5 and S6. The R curves for peeling directions 1 and 4 show periodic patterns, but those for peeling directions 2 and 3 exhibit an ascending trend with increasing crack length. Such trend is due to the relaxation of significant compressive contact between the teeth of the upper and lower surfaces behind the crack tip as the crack lengthens. The detailed discussion can be found in Section S3 and here we focus on R_{min} and the adhesion enhancement.

As Figures 11(a) and (b) show, R_{min} for peeling direction 1 always occur in the vicinity of kink C while those for the other 3 peeling directions occur in the vicinity of kink B (contrary to symmetric peeling where R_{min} for both peeling directions occur at the same location, see Figure 7(a)). As well, there are substantial differences in the R_{min} values. The adhesion enhancement factor F for the four peeling directions are shown in Figure 11(c) and (d). F for peeling direction 1 varies from 2.8 to 3.3 while that for peeling direction

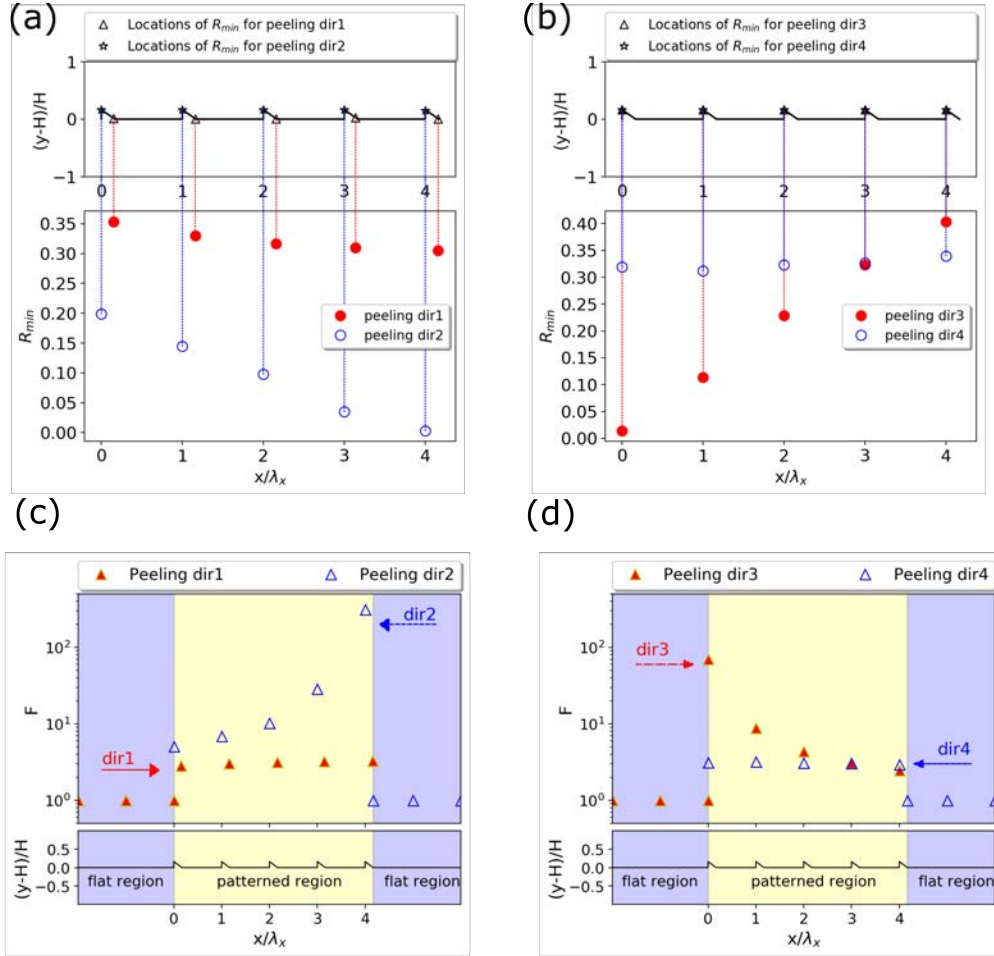


Figure 11: R_{min} for asymmetric peeling directions (a) 1 and 2 (b) 3 and 4, plotted against the normalized apparent crack tip location where R_{min} occurs. F for asymmetric peeling directions (c) 1 and 2 (d) 3 and 4, plotted against the normalized apparent crack tip location where R_{min} occurs.

2 varies in the large range of 5.0 to 312; F for peeling direction 3 varies from 2.5 to 70 while the range for peeling direction 4 is narrow, from 3.0 to 3.1. The results indicate that strong directional adhesion is achieved via different asymmetric peeling directions. Particularly, F for peeling directions 2 and 3

can reach remarkable values in the first period, although the values decrease with crack length and can eventually become comparable to or even lower than those in peeling directions 1 and 4. By contrast, F for peeling directions 1 and 4 are fairly low but steady as the crack tips propagate through the entire interface.

4. Discussion

4.1. Modulating directional adhesion with geometry

Having observed remarkable directional adhesion induced by the triangular patterned interface under peeling, we now investigate the effects of geometrical parameters on the adhesion enhancement and directional adhesion. Two non-dimensional ratios are chosen for this study: H/l and h/l . H/l represents the size of the bulk material relative to the pattern while h/l captures the influence of angle θ since $\tan(\theta) = h/l$ (Figure 1(c)). Models with different H/l and θ values are simulated by varying H and h as shown in Table 1, while keeping other geometrical parameters the same as in Section 3. Symmetric peeling as defined in Figure 1(b) is applied in all cases, and both peeling directions 1 and 2 are considered.

Table 1: Parameters for investigating the effect of H/l and θ .

parameter	value			
H/l	3.5	4	4.5	5
$\theta(^{\circ})$	20	25	30	35

Figure 12(a) shows F versus x/λ_x where R_{min} occurs, for different H/l while fixing $\theta = 30^\circ$. F for peeling direction 1 is generally lower than that for peeling direction 2, and it is insensitive to the change of H/l in this peeling direction. The slight increases in F along direction 1 as H/l increases can be seen from the enlarged inset in Figure 12(a). On the other hand, there is a notable decrease in F with increasing H/l if the crack propagates along direction 2. As a result, directional adhesion becomes weaker with increasing H/l . For example, at $x/\lambda_x = 4$, F for peeling direction 2 is ~ 6 times higher for $H/l = 3.5$ but ~ 4 times higher for $H/l = 5$.

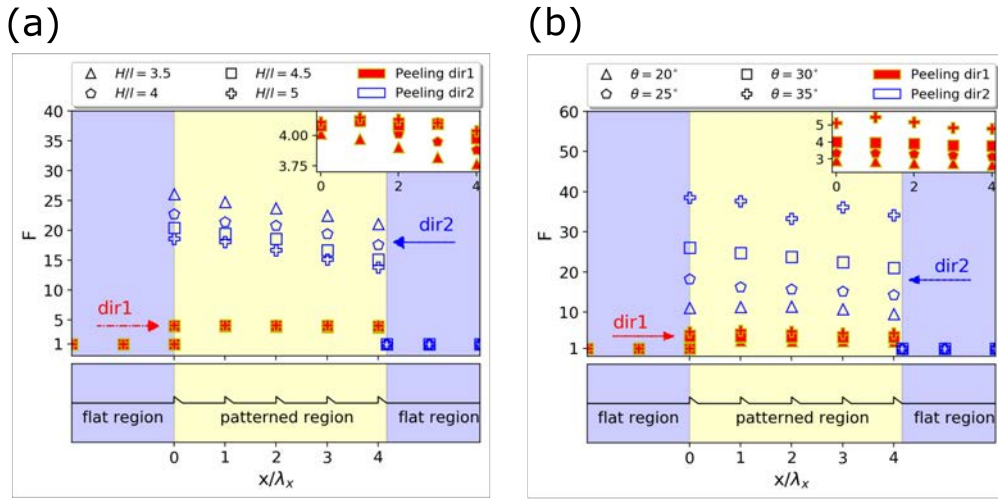


Figure 12: Adhesion enhancement factor F plotted against the normalized apparent crack tip locations where R_{min} occurs by (a) varying H/l and fixing $\theta = 30^\circ$; (b) varying θ and fixing $H/l = 3.5$. The insets plot enlarged region for F along direction 1.

The observation in Figure 12(a) can be understood by partitioning the model into “bulk” and “interface” regions (see Figure S9 in Supplementary Material). Strain energies for the two regions are computed separately to

evaluate their contribution to G and consequently R_{min} . Along direction 1, as H/l increases the contribution to R_{min} by the interface decreases whereas the contribution by the bulk increases because the volume fraction of the bulk increases. The changes in the contribution to R_{min} by the bulk and interface are of similar magnitude, which, together with the opposite trends, lead to the insensitivity of F to H/l along direction 1. Along direction 2, the contribution to R_{min} by the interface and bulk also vary with H/l in the same qualitative manner. However, the bulk contribution has larger variation with H/l . Consequently, R_{min} follows the same trend as the bulk contribution, i.e., increasing with H/l , and F in turn decreases with H/l . In addition, the contribution by the bulk has positive values and that by the interface has negative values, indicating more strain energy stored in the interface as crack propagates (Figure S10(b) in Supplementary Material). This is due to the large deformation that takes place at the triangular teeth when the crack tip reaches the vicinity of kink B , which is insignificant along direction 1 but significant along direction 2. The negative contribution by the interface also leads to the smaller magnitude of R_{min} and hence more sensitivity of $F(= \frac{1}{R_{min}})$ to H/l . More detailed discussion can be found in Section S3 in Supplementary Material.

Figure 12(b) shows F versus x/λ_x where R_{min} occurs, for different θ while fixing $H/l = 3.5$. Again, F for peeling direction 1 is generally lower than that for peeling direction 2. Besides, F for both peeling directions increase with increasing θ , with a stronger dependence of F on θ along peeling direction

2. As a result, directional adhesion becomes stronger as θ increases. For example, at $x/\lambda_x = 0$, F for peeling direction 2 is approximately 4.1 time higher for $\theta = 20^\circ$ and 7.5 times higher for $\theta = 35^\circ$.

To explain the above observations in Figure 12(b), we carefully investigated the regions in the vicinity of B in the first period when the crack tips are at B_1 and B_2 , and about to propagate to B_1^+ and B_2^+ , respectively for peeling directions 1 and 2 (see Figure 8 for the definitions of points B_1^+ and B_2^+). Similar to Section 3.2, three auxiliary simulations are performed to investigate the deformation of the upper and lower surfaces under three loading conditions: peeling only the top surface, only the bottom surface, and both. For direction 1, it was discussed in Section 3.2 that the dominant contribution to crack propagation is by peeling the upper part. As θ increases, this contribution reduces, evidenced by the reduction in crack opening as shown in Figure S11 (Supplementary Material). This leads to the reduction in $G_{pattern}$ when crack tip reaches B^+ under symmetric peeling. The same observations are made for peeling direction 2, where the dominant contribution, from peeling the lower part, decreases as θ increases (see Figure S12 in Supplementary Material). In addition, the magnitude of $G_{pattern}$ is smaller along direction 2 (see Figure S13 in Supplementary Material), giving rise to the more sensitivity of F to θ since $F = 1/R_{min} = (G_{flat}/G_{pattern})_{min}$.

Design principles to produce strong directional adhesion can be generated from a systematic parametric study. While the parameter space varies largely from one application to another, here we provide a demonstration of how to

use FEA to make design suggestions. Triangular interface model as shown in Figure 1 is subjected to symmetric peeling from directions 1 and 2. Four H/l and four θ values (Table 1) are used to create 16 cases simulated in FEA. For each case and along each direction, the adhesion enhancement factor F can vary with the apparent crack tip location where R_{min} occurs (see for example Figure 12), so the average value of F is calculated and denoted by $F_{avg,dir1}$ and $F_{avg,dir2}$ respectively for direction 1 and direction 2. The 16 values of $F_{avg,dir1}$ allow us to generate a contour plot, shown in Figure 13(a), with θ and H/l being the two variables. Linear interpolation was used to smoothen the contour. Similar contours are given in Figure 13(b) for $F_{avg,dir2}$ and in Figure 13(c) for the ratio $F_{avg,dir2}/F_{avg,dir1}$, the latter being an indicator for directional adhesion.

Upon examining Figure 13(a), $F_{avg,dir1}$ varies in the range of 2.8 to 5.2, is sensitive to θ but insensitive to H/l . In Figure 13(b), $F_{avg,dir2}$ varies in the range of 9.0 to 36.0, and is sensitive to both H/l and θ , i.e., it increases with increasing θ or decreasing H/l . Besides, the dependence of $F_{avg,dir2}$ on H/l is stronger for taller teeth (larger θ). Because $F_{avg,dir1}$ and $F_{avg,dir2}$ show different sensitivities to θ and H/l , it is possible to tune directional adhesion by modulating the two parameters. As can be seen in Figure 13(c), a strong directional adhesion, i.e., large $F_{avg,dir2}/F_{avg,dir1}$ requires a combinations of higher θ and lower H/l . One can also change $F_{avg,dir2}$ while maintaining $F_{avg,dir1}$ by keeping θ constant and varying H/l .

4.2. Applicability of results

In our FEA, several assumptions have been made on the material property and loading conditions. Here we discuss how the results might be different if some of the assumptions were changed. Firstly, we expect the results to be qualitatively similar if the material is linearly elastic instead of hyperelastic. For materials with additional dissipation mechanisms, e.g., elastic-plastic, viscous-elastic, or tough elastomer and hydrogel with damage mechanisms [24][25][26], higher adhesion enhancement is expected due to the dissipation in the bulk material. Whether directional adhesion is stronger or weaker than the case of elastic material is a more complex question, due to the potential synergistic effect of crack-trapping and bulk dissipation. While such a question can be answered by future simulations, it is more desirable to minimize bulk dissipation for the design of interface with directional adhesion to achieve better repeatability.

Secondly, we applied displacement control in our simulations. Several differences can be expected if load control were applied instead. As can be seen from the results earlier, along the patterned interface, the energy release rate G undergoes many non-monotonic changes. When G is below the intrinsic work of adhesion, the crack is trapped, and when it is above the intrinsic work of adhesion, the crack will propagate in an unstable fashion under the load control. Therefore, stick-slip behavior will be more prominent under load control. In terms of adhesion enhancement compared with a flat interface, results under symmetric peeling may not be influenced much by the change

from displacement to load control. However, in Section S3 it is discussed that under asymmetric peeling with displacement control, the compressive contact between the surfaces leads to the strain energy near the interface being stored and then released at a larger crack length, giving rise to the descending trend in adhesion enhancement with increasing crack length. Applying a fixed load condition can possibly remove the compressive contract, and hence the decreasing trend in adhesion enhancement. In practice, a 90° peeling test is commonly applied to measure adhesion [27], which can also lead to the lack of compressive contact between the surfaces. Loading conditions such as 90° peeling are typically associated with large displacement and hence numerical complications, which require more investigations in the future.

Furthermore, our FE simulations were performed by assuming plane stress. A separate FE simulation is performed with the same geometry and loading conditions as in Section 3.2, but using the plane strain assumption. The results are shown in Figure S14 (Supplementary Material), along with those using the plane stress assumption for comparison. The results are similar both qualitatively and quantitatively, indicating the insensitivity to the choice of plane stress or plane strain assumptions.

In addition, all analyses in this work are two dimensional. It is of interest to consider a three-dimensional extension of the problem where the upper and lower surfaces contain repeating prismatic versions of the triangles. The problem is certainly more complicated, since in some previous works fingering instability at the crack front has been reported [27][28][29], which can affect

the adhesion enhancement. Synthesis of such an interface may also pose a challenge, but it is a very interesting direction to pursue in the future.

Finally, our proposed interface contains only right triangles. We focused on this interfacial feature because it is effective in generating directional adhesion and would be easiest to fabricate in practice. Other triangular geometries can also be considered, but there may be difficulties in fabrication and/or other issues. For instance, if the right angle in our triangles were replaced by an obtuse angle, there would be significant crack-trapping when the crack propagates along direction 2 and possibly cohesive failure in the bulk material. Conversely if the right angle were replaced by an acute angle, we would expect smaller difference between adhesion along the two directions, i.e., weaker directional adhesion.

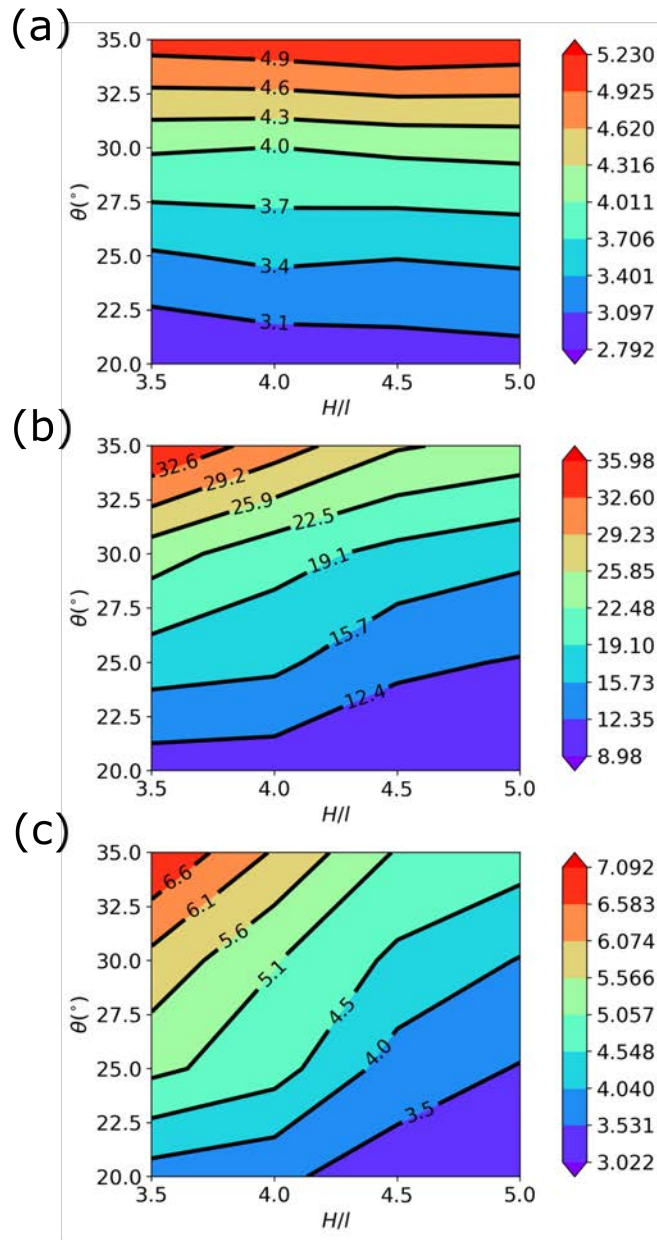


Figure 13: Contour plots for (a) the average adhesion enhancement factor along direction 1, $F_{avg,dir1}$ (b) corresponding value along direction 2, $F_{avg,dir2}$ and (c) $F_{avg,dir2}/F_{avg,dir1}$. Each contour plot is generated with θ and H/l being the two variables.

5. Conclusion

In this work, the adhesion in asymmetric patterned complementary interface is studied by FEA. The interface contains right triangles separated by flat regions. Different crack separation directions are examined under three types of loading conditions, pulling, symmetric peeling and asymmetric peeling. Compared with a flat interface, enhanced adhesion is observed along all directions under all loading conditions. Under pulling, the adhesion enhancement has very weak dependence on the direction of interface separation. Observations for models under peeling are quite different. The adhesion enhancement factor obtained by propagating the crack along opposite directions can differ by as much as two orders of magnitude, suggesting strong directional adhesion.

The effects of two non-dimensional parameters on the adhesion enhancement are systematically investigated: H/l which represents the size of the bulk sample relative to the pattern, and the angle θ in the triangle. Increase in H/l leads to weaker directional adhesion while increasing θ enhances directional adhesion. Such parametric studies can be used to guide the design of interface with desired directional adhesion.

6. Acknowledgements

The authors acknowledge financial support from Natural Sciences and Engineering Research Council of Canada (grant number: RGPIN 04281).

Reference

- [1] G. de Mestral, Velvet type fabric and method of producing the same (09 1995).
- [2] A. L. Fry, Repositionable pressure-sensitive adhesive sheet material (03 1993).
- [3] S. Kim, M. Spenko, S. Trujillo, B. Heyneman, D. Santos, M. R. Cutkosky, Smooth vertical surface climbing with directional adhesion, *IEEE Transactions on Robotics* 24 (1) (2008) 65–74.
- [4] S. Wang, M. Li, J. Wu, D.-H. Kim, N. Lu, Y. Su, Z. Kang, Y. Huang, J. A. Rogers, Mechanics of epidermal electronics, *Journal of Applied Mechanics* 79 (3) (2012) 031022–031022–6.
- [5] R. C. Webb, A. P. Bonifas, A. Behnaz, Y. Zhang, K. J. Yu, H. Cheng, M. Shi, Z. Bian, Z. Liu, Y. S. Kim, W. H. Yeo, J. S. Park, J. Song, Y. Li, Y. Huang, A. M. Gorbach, J. A. Rogers, Ultrathin conformal devices for precise and continuous thermal characterization of human skin, *Nature Materials* 12 (10) (2013) 938–944.
- [6] A. Mahdavi, L. Ferreira, C. Sundback, J. W. Nichol, E. P. Chan, D. J. D. Carter, C. J. Bettinger, S. Patanavanich, L. Chignozha, E. Ben-Joseph, A. Galakatos, H. Pryor, I. Pomerantseva, P. T. Masiakos, W. Faquin, A. Zumbuehl, S. Hong, J. Borenstein, J. Vacanti, R. Langer, J. M. Karp,

- A biodegradable and biocompatible gecko-inspired tissue adhesive, *Proceedings of the National Academy of Sciences* 105 (7) (2008) 2307–2312.
- [7] H. Lee, B. P. Lee, P. B. Messersmith, A reversible wet/dry adhesive inspired by mussels and geckos, *Nature* 448 (7151) (2007) 338–341.
- [8] C. Creton, Pressure-Sensitive Adhesives : An Introductory Course, *MRS Bulletin* 28 (6) (2003) 434–439.
- [9] K. Autumn, Y. A. Liang, S. T. Hsieh, W. Zesch, W. P. Chan, T. W. Kenny, R. Fearing, R. J. Full, Adhesive force of a single gecko foot-hair, *Nature* 405 (6787) (2000) 681–685.
- [10] A. Jagota, S. J. Bennison, Mechanics of adhesion through a fibrillar microstructure, *Integrative and Comparative Biology* 42 (6) (2002) 1140–1145.
- [11] C. Y. Hui, N. J. Glassmaker, T. Tang, A. Jagota, Design of biomimetic fibrillar interfaces: 2. mechanics of enhanced adhesion, *Journal of the Royal Society Interface* 1 (1) (2004) 35–48.
- [12] T. Tang, C.-Y. Hui, N. J. Glassmaker, Can a fibrillar interface be stronger and tougher than a non-fibrillar one?, *Journal of The Royal Society Interface* 2 (5) (2005) 505–516.
- [13] M. Sitti, R. S. Fearing, Synthetic gecko foot-hair micro/nano-structures as dry adhesives, *Journal of Adhesion Science and Technology* 17 (8) (2003) 1055–1073.

- [14] B. Aksak, M. P. Murphy, M. Sitti, Adhesion of biologically inspired vertical and angled polymer microfiber arrays, *Langmuir* 23 (6) (2007) 3322–3332.
- [15] C. Greiner, A. D. Campo, E. Arzt, Adhesion of bioinspired micropatterned surfaces: effects of pillar radius, aspect ratio, and preload, *Langmuir* 23 (7) (2007) 3495–502.
- [16] A. del Campo, C. Greiner, E. Arzt, Contact shape controls adhesion of bioinspired fibrillar surfaces, *Langmuir* 23 (20)(2007) 10235–43.
- [17] N. J. Glassmaker, A. Jagota, C.-Y. Hui, W. L. Noderer, M. K. Chaudhury, Biologically inspired crack trapping for enhanced adhesion., *Proceedings of the National Academy of Sciences of the United States of America* 104 (26) (2007) 10786–10791.
- [18] V. Shilpi, K. Krishnacharya, Y. Shu, H. Chung-Yuen, J. Anand, Adhesion selectivity using rippled surfaces, *Advanced Functional Materials* 21 (3) (2011) 547–555.
- [19] A. K. Singh, Y. Bai, N. Nadermann, A. Jagota, C.-Y. Hui, Adhesion of microchannel-based complementary surfaces, *Langmuir* 28 (9) (2012) 4213–4222.
- [20] Z. Zhang, T. Zeng, Y. Lai, M. Jia, J. Li, A comparative study of different binders and their effects on electrochemical properties of LiMn_2O_4

- cathode in lithium ion batteries, *Journal of Power Sources* 247 (2014) 1 – 8.
- [21] M. H. T. Nguyen, E.-S. Oh, Application of a new acrylonitrile/butylacrylate water-based binder for negative electrodes of lithium-ion batteries, *Electrochemistry Communications* 35 (2013) 45 – 48.
- [22] D. Chen, R. Yi, S. Chen, T. Xu, M. L. Gordin, D. Wang, Facile synthesis of graphene–silicon nanocomposites with an advanced binder for high-performance lithium-ion battery anodes, *Solid State Ionics* 254 (2014) 65 – 71.
- [23] Measurement of nonlinear mechanical properties of pdms elastomer, *Microelectronic Engineering* 88 (8) (2011) 1982 – 1985.
- [24] M. L. Oyen, R. F. Cook, Load–displacement behavior during sharp indentation of viscous–elastic–plastic materials, *Journal of Materials Research* 18 (1) (2003) 139–150.
- [25] E. Ducrot, Y. Chen, M. Bulters, R. P. Sijbesma, C. Creton, Toughening elastomers with sacrificial bonds and watching them break, *Science* 344 (6180) (2014) 186–189.
- [26] J. Y. Sun, X. Zhao, W. R. Illeperuma, O. Chaudhuri, K. H. Oh, D. J. Mooney, J. J. Vlassak, Z. Suo, Highly stretchable and tough hydrogels, *Nature* 489 (7414) (2012) 133–6.

- [27] H. Yuk, T. Zhang, S. Lin, G. A. Parada, X. Zhao, Tough bonding of hydrogels to diverse non-porous surfaces, *Nat Mater* 15 (2) (2016) 190–6.
- [28] A. Ghatak, M. K. Chaudhury, V. Shenoy, A. Sharma, Meniscus instability in a thin elastic film, *Phys. Rev. Lett.* 85 (2000) 4329–4332.
- [29] J. S. Biggins, B. Saintyves, Z. Wei, E. Bouchaud, L. Mahadevan, Digital instability of a confined elastic meniscus, *Proceedings of the National Academy of Sciences* 110 (31) (2013) 12545–12548.